

1 **Implementation and application of an improved phase spectrum** 2 **determination scheme for Fourier Transform Spectrometry**

3 Frank Hase¹, Paolo Castracane⁵, Angelika Dehn⁵, Omaira Elena García⁷, David W. T. Griffith³, Lukas
4 Heizmann⁶, Nicholas B. Jones³, Tomi Karppinen⁴, Rigel Kivi⁴, Martine de Mazière², Justus Notholt⁶,
5 Mahesh Kumar Sha²

6

7 ¹IMKASF, Karlsruhe Institute of Technology (KIT), Eggenstein-Leopoldshafen, 76344, Germany

8 ²Royal Belgian Institute for Space Aeronomy (BIRA-IASB), Ringlaan 3, 1180 Brussels, Belgium

9 ³University of Wollongong, Wollongong, Australia

10 ⁴Space and Earth Observation Centre, Finnish Meteorological Institute, Sodankylä, Finland

11 ⁵European Space Agency, ESA/ESRIN, Frascati RM, Italy

12 ⁶Institute of Environmental Physics, University of Bremen, Bremen, Germany

13 ⁷Izaña Atmospheric Research Centre (IARC), State Meteorological Agency of Spain (AEMet), Santa Cruz de Tenerife,
14 Spain

15 *Correspondence to:* Frank Hase (frank.hase@kit.edu)

16 **Abstract.** Correct determination of the phase spectrum is a highly relevant task in Fourier Transform Spectrometry for
17 concluding which spectral distribution most likely gave rise to the measured interferogram. We present implementation of
18 an improved scheme for phase determination in the operational Collaborative Carbon Column Observing Network
19 (COCCON) processor. We introduce a robust unwrapping scheme for retrieving a spectrally smooth phase spectrum at
20 intermediate spectral resolution, which uses all spectral positions carrying enough signal to allow a significant determination
21 of the phase. In the second step, we perform a least squares fit of model parameters of a suitable analytical phase spectrum
22 model through all reliable phase values constructed in the first step. The model fit exploits the fact that we expect the phase
23 to be spectrally smooth. Still, it can be refined to reflect specific characteristics inherent to the optical and electronic layout
24 of the interferometer. The proposed approach avoids the problems of the classical phase reconstruction method, which
25 enforces a spectrally smooth phase by directly limiting spectral resolution when calculating the complex phase. Thereby, the
26 phase is created from a very low number of interferogram points around the centerburst of the interferogram, which results in
27 a suboptimal noise propagation from the interferogram into the spectral domain. Moreover, the interpolation of the phase
28 spectrum across spectral subsections with reduced spectral signal is not well behaved and results depend strongly on the
29 numerical apodization function used for creating the low-resolution phase.

30 **1 Introduction**

31 Fourier Transform Spectrometry is an important technique for remote observation of atmospheric composition, especially in
32 the near and mid infrared spectral regions, where it is mostly referred to as Fourier Transform Infra-Red (shortened to FTIR)
33 spectrometry. Ground-based networks contribute to the long-term monitoring of chemical composition, as the Network for
34 the Detection of Atmospheric Composition Change (NDACC) network [De Mazière et al., 2018], and the Total Carbon
35 Column Observing Network (TCCON) [Wunch et al., 2011] and the COLlaborative Carbon Column Observing Network
36 (COCCON) [Frey et al., 2019; Sha et al., 2020; Alberti et al., 2022], which focus on the provision of precise and accurate
37 observations of column-averaged greenhouse and other climate and air quality relevant gas abundances. The first high-
38 resolution FTS in space was the Atmospheric Trace Molecule Spectroscopy (ATMOS) experiment on the Space Shuttle
39 [Farmer, 1987]. Moreover, highly successful space borne sensors as Michelson Interferometer for Passive Atmospheric
40 Sounding (MIPAS) onboard the Environmental Satellite (ENVISAT) [Fischer et al., 2008], Atmospheric Chemistry
41 Experiment – Fourier Transform Spectrometer (ACE-FTS) onboard SCISAT [Bernath and al., 2005], and the Thermal And
42 Near infrared Sensor for carbon Observation – Fourier Transform Spectrometer (TANSO-FTS) onboard Greenhouse gases
43 Observing SATellite (GOSAT) [Yokota et al., 2009] and its successors have proven the usefulness of FTIR spectrometry for
44 atmospheric observations. Recently, the airborne imaging FTIR sensor Gimballled Limb Observer for Radiance Imaging of
45 the Atmosphere (GLORIA) for chemical and thermal limb imaging has been realized [Friedl-Vallon et al., 2014] and the
46 imaging FTIR satellite mission Changing Atmosphere Infrared Tomography (CAIRT) derived from GLORIA is under phase
47 A study by ESA [<https://www.cairt.eu>].

48 All FTIR spectrometers have in common that they use a two-beam interferometer for creating modulated intensity levels as a
49 function of the path difference between the two arms of the interferometer. The path difference is varied as function of time,
50 and during such a scan, the variable intensity is recorded by a detector element. By use of a co-recorded reference
51 modulation generated from a reference laser fed through the same interferometer, the variable intensity level recorded by the
52 infrared detector as function of time can be sampled as function of optical path difference x . It can be shown that the Fourier
53 Transform of the AC-coupled interferogram is associated with the spectral distribution of the incident radiation. If the
54 interferogram $I(x)$ would be symmetric around a common zero path difference (ZPD) of the interferometer for any
55 wavenumber ν , the spectral radiance as function of wavenumber $S(\nu)$ would be connected with the interferogram via a
56 simple cosine transform:

57

$$58 \quad S(\nu) = \int_{x=-\infty}^{+\infty} I(x) \cos(2\pi\nu x) dx \quad (1)$$

59

60 We only claim a proportionality here for any selected wavenumber position, because from the practical viewpoint, the
61 determination of radiances in absolute units requires proper calibration measurements using reference sources providing a
62 known radiance level. This is a very laborious task and it is difficult to achieve sub-percent accuracy in the realization of

63 absolute units. In case of emission spectrometry, this task needs to be solved, while atmospheric absorption spectrometry
64 generally omits this procedure. In the case of absorption spectrometry, the quantitative trace gas analysis is built on the local
65 contrast between absorption lines and adjacent continuum (assuming that the spectrometer offers sufficient spectral
66 resolution for resolving individual lines). Then, by assuming that the spectrally variable sensitivity of the spectrometer,
67 created by optical, detector, and electronic characteristics is spectrally smooth, no attempt is made for achieving ordinate
68 calibration. A section of the measured spectrum used for the trace gas analysis is then treated as a transmission spectrum, and
69 an empirical fit of continuum background is included in the analysis scheme. We do not further follow the problem of
70 ordinate calibration here, because it is not related to our aim of an improved phase reconstruction, which, however, can be
71 used for both absorption and emission spectrometry.

72

73 In equation (1), we have extended the integration over all optical path differences. In practice, only a limited section up to a
74 maximum optical path difference (MPD) is accessible. The truncation of the interferogram is equivalent to a multiplication
75 with a boxcar function. In spectral domain, this becomes a convolution with a sinc function. The spectral response inherent
76 to an FTIR spectrometer is called instrumental line shape (ILS). It can be adjusted by applying a numerical weighting
77 function along the interferogram (the process of apodization). Especially, numerical apodization allows to dampen the
78 sidelobes of the sinc function, which allows – at the cost of widening the ILS width – to suppress the ringing surrounding
79 unresolved spectral lines. A proper description of the instrumental line shape (ILS) is further complicated due to the presence
80 of practical imperfections of the interferometer as misalignment of optical components or mechanical imprecision of the
81 scanning mechanism [Hase et al., 1999]. Finally, we do not further follow the problem of spectral ordinate calibration here,
82 because it, too, is not closely related to our aim of an improved phase reconstruction.

83

84 In order to provide a proper idea of the practical method of FTIR spectroscopy here, we further need to mention that the data
85 recording and processing is digital. An analogue-to-digital (ADC) converter is used to generate a digitized signal from the
86 detector signal. While sample-and-hold ADCs triggered by the laser sampling were used in the past, many manufacturers of
87 FTIR spectrometers today use widely available audio ADCs which offer high digitization depth (e.g. 24 bit) and add a final
88 interpolation step from the raw sampling equidistant in time domain into a sampling record equidistant in space [Brault,
89 1996]. In any case, the signal to be processed is discretely sampled, and in practice fast computational schemes for doing
90 discrete Fourier transforms are applied. Due to the discrete sampling process, integrals as shown in equation (1) become
91 sums and the bandwidth of the recorded signal needs to be properly limited in order to avoid aliasing.

92

93 A final aspect, which is closely connected to the considerations developed hereinafter, is the origin of the phase spectrum.
94 Due to residual optical asymmetry of the beamsplitter unit (especially due to a potential mismatch of the substrate carrying
95 the beam-splitting layer system and the compensation plate) and possibly between the arms of the interferometer and due to
96 frequency dependent electronic delays, the resulting interferogram tends to be asymmetric and a global ZPD position

97 common to all wavenumbers does not exist. The electronic delays introduce both a shift between the laser reference and the
 98 signal, as well as frequency-dependent delays in the infrared signal. This requires treatment of the Fourier Transform of the
 99 real-valued interferogram as a complex quantity (so arising out of cosine and sine contributions) and thereby gives birth to
 100 the concept of the phase spectrum. In complex notation, we can state

$$102 \quad s(\nu) = |s(\nu)|e^{i\varphi(\nu)} = \int_{x=-\infty}^{+\infty} I(x)e^{-i2\pi\nu x} dx \quad (2)$$

103
 104 The uncalibrated signal $s(\nu)$ now is a complex quantity. It can be separated into amplitude and phase $\varphi(\nu)$. The phase
 105 spectrum $\varphi(\nu)$ describes how the phase angle of the harmonic oscillations which make up the interferogram evolves as
 106 function of wavenumber. From the instrumental viewpoint, we expect the phase spectrum to be spectrally smooth, as the
 107 impacting factors (optical dispersion and electronic delays) typically vary slowly as function of frequency.

108
 109 The smoothness of the phase spectrum in near and mid-infrared FTIR spectrometry is verified empirically on scales of
 110 several to tens or even hundreds of wavenumbers (cm^{-1}). Given this, the simple approach of interpreting the absolute value of
 111 the resulting complex spectrum as the measured spectral signal is clearly suboptimal in the presence of noise in the
 112 interferogram. The assumption of uncorrelated white noise typically is adequate for interferogram samples. This noise maps
 113 into white noise in the complex spectrum. A contribution of $1/f$ noise might increase the noise amplitude towards low
 114 frequencies, and at very low frequencies, source noise might become dominant. Therefore, working at higher scan speeds is
 115 generally preferred.

116
 117 The assumption of a spectrally smooth phase allows separation of the complex spectrum into two orthogonal components:
 118 the component along the direction in the complex plane we expect the spectral signal to be oriented, and the component
 119 orthogonal to this direction. So, by exploiting the concept of a spectrally smooth phase, the noise mapped into the orthogonal
 120 component can be avoided, only the noise along the signal component is unavoidable. Moreover, this approach avoids the
 121 spectral noise floor of becoming a positive bias in opaque spectral subsections, as it would occur when simply using the
 122 absolute value of the complex spectrum.

123
 124 In order to make the scheme of a smooth phase a working concept, we not only rely on the assumption that it actually is
 125 spectrally smooth, but we also need a practical approach for constructing a smooth phase spectrum with a noise level
 126 significantly below the noise level of the complex spectrum. In practice, we achieve this by using only a short section of the
 127 interferogram around ZPD. Thereby, the smooth phase spectrum is set by the equation

$$129 \quad |s(\nu) \otimes FT(A_{trunc})|e^{i\varphi(\nu)} = \int_{x=-\varepsilon \cdot MPD}^{+\varepsilon \cdot MPD} I(x)e^{-2\pi\nu x} \cdot A(x) dx \quad (3)$$

130

131 Here, the dimensionless multiplier ε denotes that only a fraction of the complete interferogram recorded up to MPD is used.
132 The function $A(x)$ denotes a strong numerical apodization function, as any non-local ringing extending out from a spectral
133 position with high signal level would disturb the phase in the surrounding spectral region. The spectral signal $s(\nu)$ generally
134 is spectrally structured, so reducing the interferogram to the narrow range of $-\varepsilon \cdot MPD$ to $+\varepsilon \cdot MPD$ convolves the spectral
135 signal with the Fourier transform of the truncated apodization function A_{trunc} .

136

137 We finally need to mention that interferograms might be recorded “single-sided” or “double-sided”. Often, when an
138 interferometer is designed for achieving higher spectral resolution, the symmetry of the design is abandoned. Instead, the
139 ZPD position is shifted to be near one end of the mechanical scan range, which still needs to be wide enough to reconstruct
140 the phase spectrum via equation (3), but the high-resolution details are inferred from the single remaining side of the
141 interferogram which is recorded. Our proposed method can be used in either situation, but it should be noted that in case of
142 single-sided interferogram recording, the error propagation of a residual phase error is much more critical, as sine
143 contributions do not cancel out (as one side of the interferogram is missing) [Brault, 1996; Brasunas and Cushman, 1997], so
144 a very accurate reconstruction is even more relevant in this case.

145

146 The reader finds detailed presentations of all the aspects of FTIR spectroscopy shortly summarized above in text books and
147 articles [Herres and Gronholz, 1985; Davis et al., 2001; Griffiths et al., 2007].

148

149 In section 2, we present the types of spectrometers we used to test the proposed phase correction method. Section 3 describes
150 a robust scheme for phase unwrapping and the fitting procedure for retrieving the parameters of the phase model. Section 4
151 investigates the characteristics of phase spectra for the spectrometers introduced in section 2.

152 **2 Materials and Methods**

153 This work has been performed in the framework of the FRM4GHG project (Fiducial Reference Measurements for
154 Greenhouse Gases; <https://frm4ghg.aeronomie.be/>) supported by European Space Agency (ESA) [Sha et al., 2020]. In the
155 framework of this project, among further topics related to fiducial reference measurements (FRM), the adequacy of different
156 portable spectrometers is investigated. For this purpose, extended measurement campaigns with the portable spectrometers
157 under test are performed at the Sodankyla site operated by the Finnish Meteorological Institute. At this site, also regular
158 aircore measurements are executed, which provide in-situ measurements of Greenhouse Gas profiles. The IFS125HR FTS
159 operated by FMI at the Sodankyla site in the framework of TCCON serves as reference. Further details of the campaign
160 setup are provided by Sha et al., 2020. Interferograms recorded with these portable spectrometers have been used for testing

161 the proposed phase reconstruction algorithm. We shortly present these spectrometers in the following. Table 1 summarizes
162 the main design characteristics of the spectrometers from the viewpoint of the phase spectrum.
163

164 The EM27/SUN Fourier-transform spectrometer (FTS) prototype has been developed by Karlsruhe Institute of Technology
165 (KIT) in cooperation with Bruker Optics, a well-known manufacturer of FTIR spectrometers. It uses a folded pendulum-
166 corner cube interferometer (“RockSolid” ® design) and employs two room temperature InGaAs detectors to cover the near-
167 infrared range from 4000 – 12 000 cm^{-1} . A solar tracker using Camtracker active feedback to control the position of the solar
168 image on the fieldstop of the spectrometer is directly attached to the spectrometer [Gisi et al., 2011]. Further instrumental
169 details of the EM27/SUN FTS design characteristics are provided by Gisi et al. (2012) and Hase et al. (2016). As an
170 operational framework for guaranteeing common instrumental and data analysis standards among the operators, the
171 COCCON has been established since [Frey et al., 2019; Alberti et al., 2022], which is significantly supported by ESA
172 through FRM4GHG and further contracts.
173

174 The Bruker IRCube or “Matrix” FTIR is a compact OEM instrument operating in the mid or near IR regions and configurable
175 for a wide range of laboratory and industrial applications using a range of sampling accessories. In its basic form it contains
176 a folded pendulum-corner cube interferometer similar to the EM27/SUN (“RockSolid” ® design) with 25mm beam diameter
177 and either 1 cm^{-1} double-sided or 0.5 cm^{-1} single-sided resolution. As used at the University of Wollongong for solar
178 measurements, the interferometer is configured for 0.5 cm^{-1} single-sided resolution.
179

180 The Vertex70 spectrometer is produced and sold commercially by Bruker Optics. It was recently replaced in Bruker’s
181 production line by a successor named Invenio. One Vertex70 FTS was purchased in the framework of the FRM4GHG
182 campaign to be tested alongside the EM27/SUN and IRCube with the reference IFS125HR and AirCore measurements. The
183 Royal Belgian Institute of Space Aeronomy (BIRA-IASB) and the University of Bremen (UB) performed minor
184 modifications to the optical components of the Vertex70 and coupled it with a solar tracker to perform solar absorption
185 measurements. The feasibility to accommodate two detectors (InGaAs and InSb) in the spectrometer allows covering
186 simultaneously the near- and mid-infrared (NIR and MIR) spectral regions. The measured spectra are analysed to retrieve
187 column abundances of XCO₂, XCH₄, XCO and XH₂O in the NIR spectral region and column abundances of methane (CH₄),
188 nitrous oxide (N₂O), formaldehyde (HCHO) and carbonyl sulphide (OCS) in the MIR spectral region are currently studied
189 [Zhou et al., 2023; Sha et al., 2024
190

191 The Izaña Observatory (IZO) is a high-mountain station located on the island of Tenerife (Canary Islands, Spain) in the
192 subtropical North Atlantic Ocean (28.3°N, 16.5°W) at an altitude of 2.37 km a.s.l. IZO is managed by the Izaña Atmospheric
193 Research Centre (IARC, <https://izana.aemet.es/>, last access: 5 August 2024), which belongs to the State Meteorological

194 Agency of Spain (AEMet). An IFS125HR spectrometer is operated for TCCON and NDACC [Schneider et al., 2010; García
195 et al., 2021].

196

197

198 Table 1: FTIR spectrometers used for investigating phase spectra characteristics

Bruker type designation	Beamsplitter design	Interferogram shape	Maximum spectral resolution (0.9/MPD) [cm ⁻¹]
EM27/SUN	Self-compensating single plate	Double-sided	0.5
IRCube	Compensated, substrate plate and air-spaced compensating plate	Single-sided	0.5
Vertex70	Compensated, substrate plate and air-spaced compensating plate	Single-sided	0.25
IFS125HR	Compensated, substrate plate and air-spaced compensating plate (both wedged)	Single-sided	< 0.005

199

200

201

202 **3 New Phase reconstruction scheme**

203 The drawback of the classical method described in the introduction is twofold. (1) The reduction of the phase spectrum to the
204 desired very low resolution is achieved explicitly by using a very short section of the interferogram around ZPD for the
205 Fourier transform [Mertz, 1965; Forman et al., 1966]. This approach neglects interferogram data points further out which
206 still could contribute information on the phase. (2) The resulting spectral interpolation as part of the procedure is not well-
207 defined especially across spectral sub-regions of increased opacity, as they occur in solar absorption spectrometry between
208 the atmospheric window regions and in strong absorption bands. Because the phase spectrum across such a region is strongly
209 impacted by the overlapping contributions to the phase emerging from either side of the opaque region, the outcome for the
210 phase at a certain spectral position in the region with reduced transmission will depend on the user-selected resolution for the
211 phase calculation and the chosen apodization function.

212

213 We will achieve our enhanced reconstruction of the phase spectrum by fitting a smooth parameterized phase model through a
214 calculated phase spectrum, which preserves higher spectral resolution than required for the desired degree of spectral
215 smoothness. The smoothness of the phase spectrum is ensured by the phase model used, while avoiding the aforementioned
216 problems of the classical method. We use a least squares fit of the model to the raw phase spectrum, which is a well-defined
217 process with respect to interpolation. A similar method has been proposed by Learner et al., 1995, in the context of emission

218 spectra. The method described in the following consists of two partial steps: First, we need to establish a procedure for
 219 constructing a smooth phase spectrum from the complex spectrum. We refer to this step as “phase unwrapping”. The
 220 trigonometric functions connecting phase angle and complex spectrum are periodic, and direct use of inverse functions
 221 would generate phase jumps. In the second step, we fit the phase values of an analytical phase model to the smooth phase
 222 spectrum generated in the first step by adjusting the chosen model parameters.

223

224 The phase spectrum is a function of angular orientation, so it is invariant under phase shifts of size $\pm 2\pi n$, with $n = 1, 2, 3, \dots$
 225 For our fit procedure, we need to ensure that the raw phase used as input does not include jumps between such branches. We
 226 suggest the very robust procedure summarized as procedural steps in Table 2.

227 This proposed method can fail if the phase difference calculated in step 5 is greater than $\pm\pi$. We did not encounter this
 228 situation, but it may occur if the phase slope is very steep and can possibly be avoided by appropriate repositioning of the
 229 ZPD point when calculating the Fourier Transform. For generating a phase point of the raw unwrapped phase, the spectral
 230 amplitude is required to exceed the adjustable threshold value T . It should be chosen well above the noise level of the
 231 complex spectrum used for the phase determination. Otherwise, the phase difference between adjacent points could
 232 occasionally exceed the requirement of phase differences to reside within the $\pm\pi$ range. Moreover, the phase in nearly
 233 opaque spectral sections can be dominated by spurious signals (originating from, e.g., nonlinearity, double-passing, or
 234 sampling ghosts), so it is desirable to exclude these spectral sections from the calculation of the analytical phase anyway.

235

236 Table 2: step-by-step procedure for the phase unwrapping algorithm, which develops the raw phase used as input for the
 237 model fit.

Step #	Procedure	Comment
0	Allocation of arrays: (1) complex float array for storing the complex spectrum s (2) float array for accepting phase values φ (3) logical array indicating validity of phase value $LVALID$	Initialize
1	Establish the noise level and the size of potential artefacts superimposed on the spectral signal. Set a threshold T for the subsequent phase calculation significantly above noise and artefact levels. Initialize all elements of the logical array: $LVALID = false$	
2	Search for position of max amplitude of $s(v_i)$ in the complex signal in the optical bandpass.	Restrict search to relevant optical bandpass, as out-of-band artefacts triggered by source brightness fluctuation

		might create very big amplitudes at $\nu \approx 0$.
3	Calculate phase $\varphi(istart)$ at spectral index $istart$ with max signal amplitude. Set <i>LVALID</i> of the position $istart$ to true. Initialize the position j , which marks the nearest preceding position with valid phase entry used in steps 5 and 6. Initialize the current position i .	Use a quadrant-sensitive <i>atan2</i> function on real and imaginary part of the complex signal. Initialize index values j and i : $j = istart$ $i = istart$
4	Move from current position one spectral index up. If still within the defined spectral bandwidth, check whether $s(\nu_i) > T$. If so, set the <i>LVALID</i> value of current position i to <i>true</i> , otherwise to <i>false</i> .	Increment index i : $i = i + 1$ If $s(\nu_i) > T$ then $LVALID(\nu_i) = true$
5	If the <i>LVALID</i> value of the current position i is <i>true</i> , calculate the phase difference between the nearest preceding point j assigned <i>LVALID</i> = <i>true</i> and the current position.	Use the value of the cross product between the normalized vectors in the complex plane: $\Delta\varphi(j \rightarrow i) = asin \left\{ \frac{(s(\nu_j) \times s(\nu_i))}{ s(\nu_j) s(\nu_i) } \right\}$
6	If the <i>LVALID</i> value of the current position i is <i>true</i> , calculate the new $\varphi(i)$ at the current position using the phase value of the nearest preceding point	$\varphi(i) = \varphi(j) + \Delta\varphi(j \rightarrow i)$
7	If the <i>LVALID</i> value of the current position i is <i>true</i> , update the value of j .	$j = i$
8	Continue steps 4 + 5 + 6 + 7 until the upper limit of the spectral bandwidth is reached.	
9	Return to position $istart$ and use the corresponding procedure in downwards direction until the lower limit of the spectral bandwidth is reached.	

238

239

240 The second step is to fit the parameters of the analytical phase model to the raw phase values. We assume here use of a
241 model linear in the model parameters to be fitted. However, nonlinear models also can be handled in our approach by
242 implementing an iterative search for the optimal model parameter values. If a sophisticated model is chosen, which intends
243 to describe actual physical characteristics of the spectrometer (dispersion curves, electronic response characteristics) and
244 retrieves physical quantities (layer thicknesses, capacitances, resistor values), using a model which is nonlinear in the

245 parameters might be unavoidable. When constructing ad-hoc models, which simply enforce smoothness, the choice of a
 246 simple linear model seems advisable. The fitting procedure needs to be restricted to points for which valid phase values were
 247 established in the previous step. The fitting procedure can take into account a weighting according to the squared signal
 248 amplitude. We found very little effect of including this refinement in the determination of model parameters, so we did not
 249 implement it in the current pre-processing scheme. Taking a weighting into account, the equation for fitting the phase model
 250 parameters becomes

$$252 \vec{p}_{model} = (K^T W K)^{-1} K^T W \vec{\varphi}_{raw} \quad (4)$$

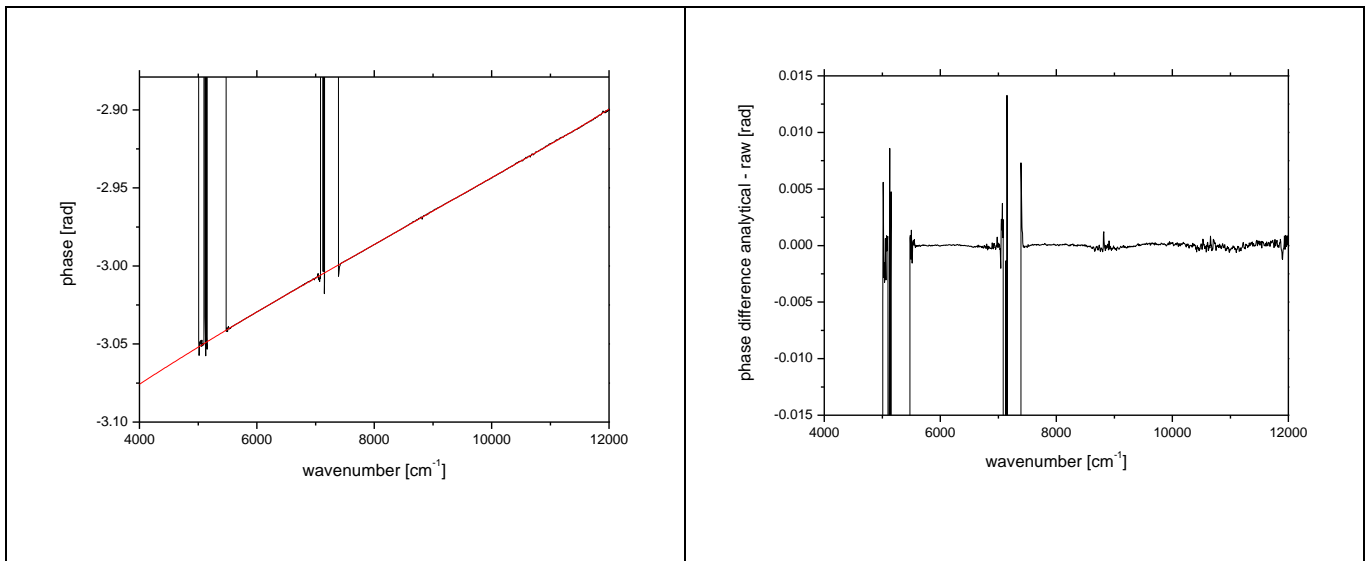
253
 254 Here, \vec{p}_{model} is the set of model parameters, K is the Jacobean matrix, which holds the derivatives of the phase model at each
 255 spectral grid point with valid raw phase entry, W is a diagonal matrix with $\frac{1}{(s(v_i))^2}$ entries (again, for each spectral grid point
 256 with valid raw phase entry), and $\vec{\varphi}_{raw}$ is the vector containing all valid raw phases. Note that the vector dimension of $\vec{\varphi}_{raw}$
 257 and \vec{p}_{model} differ, as after receiving the set of model parameters, $\vec{\varphi}_{model}$ can be calculated at all spectral positions, including
 258 interpolation across near opaque spectral sections and extrapolation beyond the first or last spectral point found in the optical
 259 bandpass. The predicted model phase values further outside of the relevant spectral bandpass are meaningless and might be
 260 suppressed altogether (by allocating the array for \vec{p}_{model} to fit the relevant spectral bandpass).

261 **4 Results**

262 For the actual work on the FTIR spectrometers introduced in section 2, we used a polynomial model of order 7. The raw
 263 phase calculation uses 3000 interferogram points on either side of ZPD, equivalent to a resolution of about 10 cm^{-1} , which
 264 is supported by all spectrometers we included in the study (sufficient number of points on the short side of the
 265 interferogram).

266 **4.1 Phase spectrum of the EM27/SUN FTS**

267 The results achieved for the EM27/SUN are shown in Figure 1. The spectrometer shows a remarkably linear phase spectrum
 268 across the whole spectral region of the main detector (covering 5000 to 12000 cm^{-1}). The differences between the model fit
 269 and the raw phase are below 1 mrad. The level of smoothness and linearity of the phase spectrum is outstanding among all
 270 spectrometers tested. This behaviour probably is supported by the beamsplitter design. The same optical plate is passed twice
 271 by the radiation, acting as substrate of the beam-splitting coating layer in one passage and as compensating plate in the other
 272 passage. In addition to this, also the analogue electronic chain seems to introduce only minimal dispersion due to runtime
 273 effects. It is not clear why the other spectrometers investigated here, all built by the same manufacturer, show significantly
 274 stronger structures in the phase spectrum.

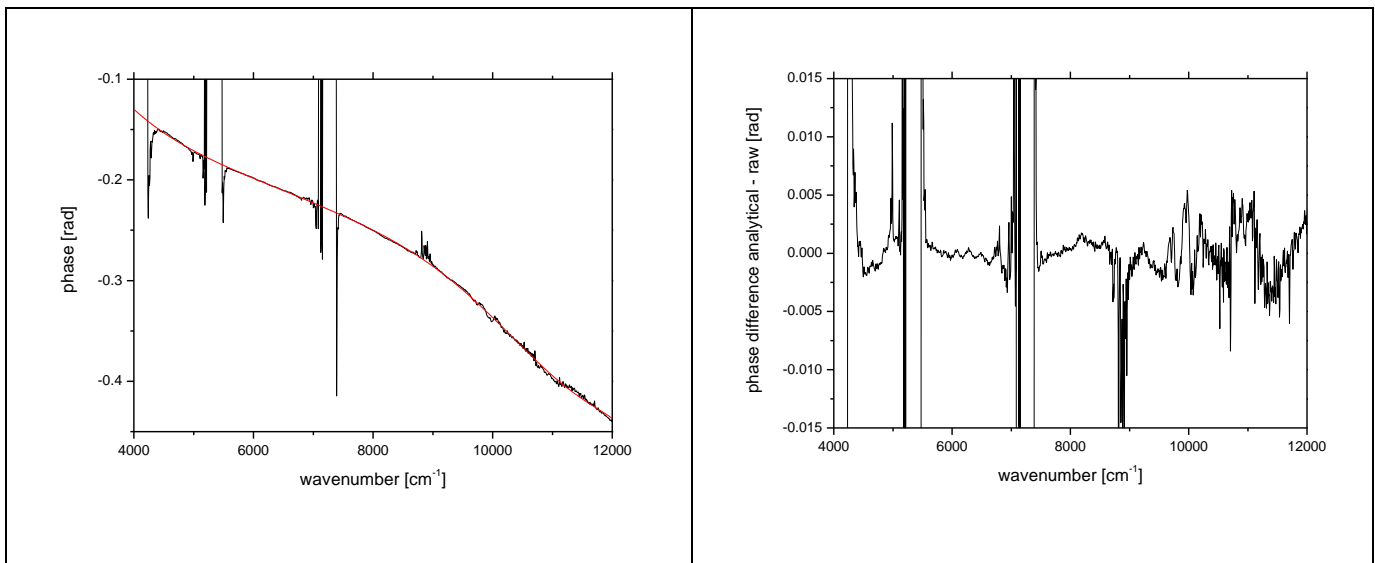


275

276 Figure 1: EM27/SUN phase spectrum. Left panel: raw phase (black) and fitted analytical phase (red). Right panel: difference
 277 between model (analytical) and raw phase (raw). The gaps in the raw phase are due to opaque spectral sections.

278 4.2 Phase spectrum of the IRCube FTS

279 The phase spectrum of the IRCube is shown in Figure 2. The spectral bandpass covers the range of 4000 to beyond 12 000
 280 cm⁻¹. The differences between the phase model and the raw phase show more structure than in case of the EM27/SUN, but
 281 still, these oscillatory features are largely within 2 mrad.

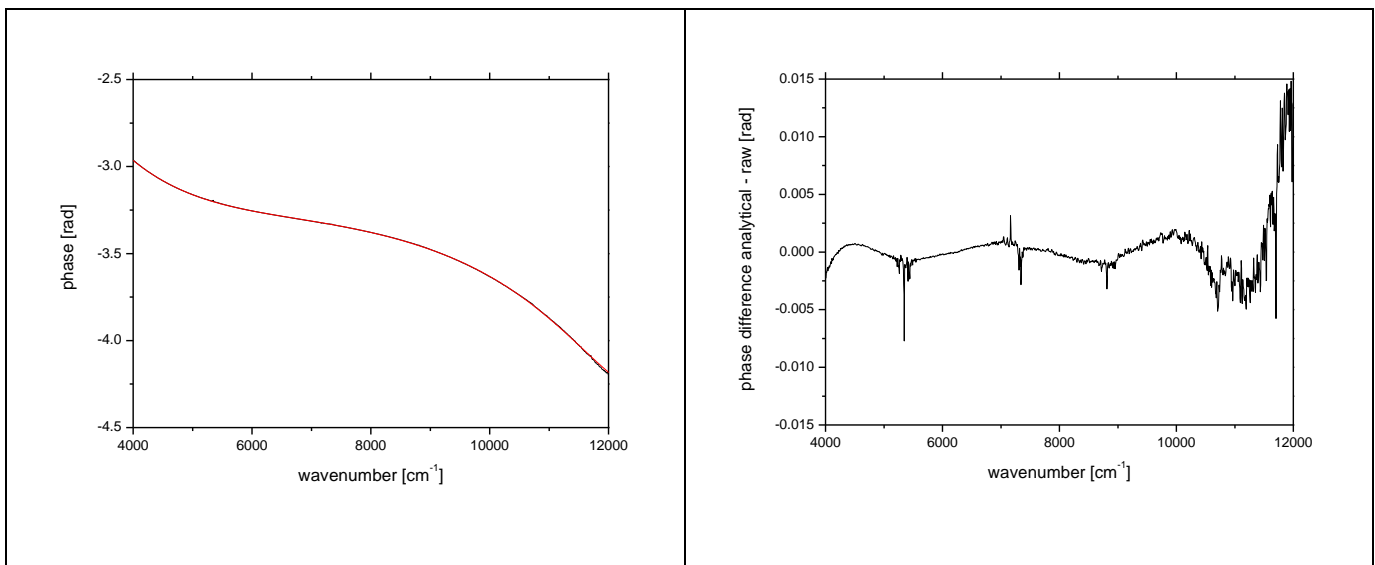


282

283 Figure 2: IRCube phase spectrum. Left panel: raw phase (black) and fitted analytical phase (red). Right panel: difference
284 between model (analytical) and raw phase (raw). The gaps in the raw phase are due to opaque spectral sections.
285

286 4.3 Phase spectrum of the IFS125HR FTS operated at Izaña

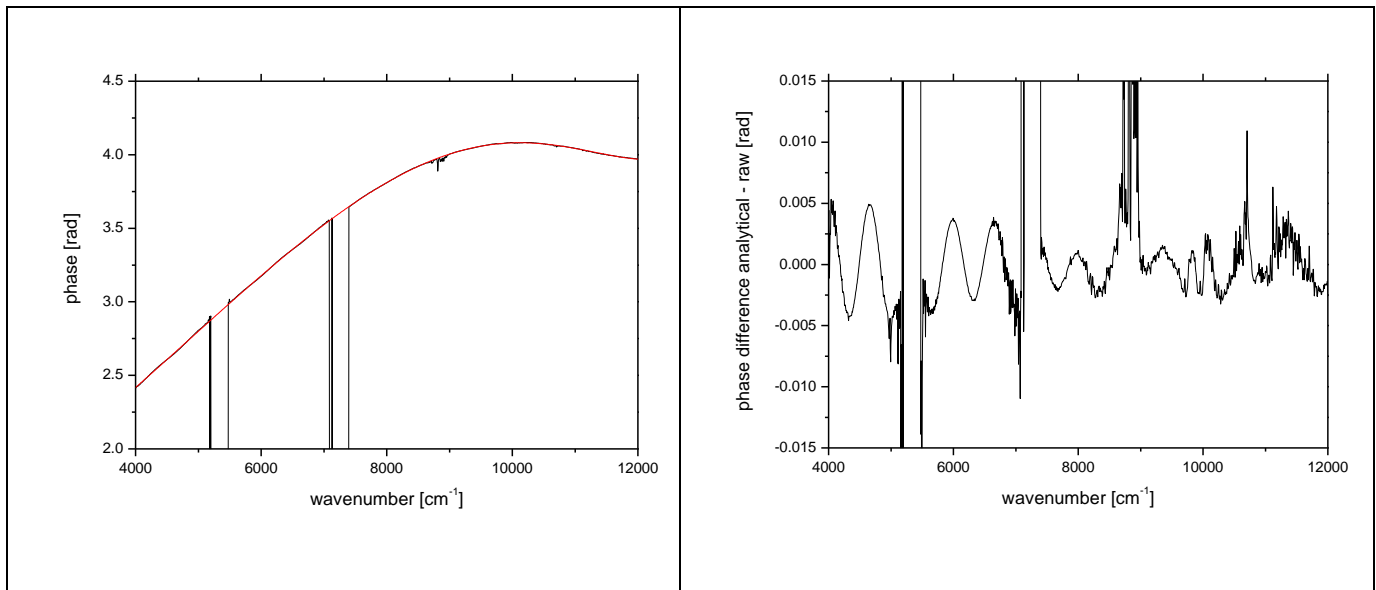
287 The phase spectrum of the IFS125HR operated at the Izaña observatory is shown in Figure 3. The spectral bandpass covers
288 4000 to beyond 12 000 cm^{-1} . Due to the facts that Izaña is a high-altitude site and a low threshold value for the phase
289 calculation was used because of the very low noise level of the measurements, there are no gaps in the raw phase. Some
290 structure can be seen in the model minus raw phase difference, but this is still within mostly 2 mrad apart from the highest
291 wavenumbers. The curvature of the phase is somewhat stronger than in the case of the IRCube. The sharp peaks occurring
292 around 5400 and 7200 cm^{-1} are coinciding with near-opaque regions of the spectrum and might hint at superimposed
293 spurious signals, potentially due to residual nonlinearity. Such spurious signals generally possess a phase orientation
294 different from the real signal. This finding demonstrates that the model-fitting approach presented here might also be useful
295 for detecting different kinds of imperfections in measured spectra.



296
297 Figure 3: IFS125HR phase spectrum. Left panel: raw phase (black) and fitted analytical phase (red). Right panel: difference
298 between model (analytical) and raw phase (raw).

299 4.4 Phase spectrum of the Vertex 70 FTS

300 Figure 4 shows the phase spectrum of the Vertex 70 FTS. The spectral range covered extends from around 4000 to beyond
301 12 000 cm^{-1} . It is the most unusual phase spectrum we found, showing pronounced quasi-periodic oscillations of about 600
302 cm^{-1} cycle length in the raw phase (see right panel), which cannot be fitted by the polynomial model used. The amplitude of
303 these oscillations amounts to ± 5 mrad. A very similar oscillatory structure is present in the successor of this spectrometer
304 offered by Bruker under the model name Invenio (not shown here). We reported back our findings to the manufacturer, but
305 so far no explanation or remedy for the unusual behaviour was found. Again, it turns out that the approach presented here to
306 fit a smooth model phase to the raw phase is useful for discovering such instrumental characteristics which otherwise remain
307 overlooked. If the approach presented here is to be applied in an operational way for Invenio measurements, a specific model
308 extension must be designed that allows to reproduce the oscillatory features found in the raw phase.
309

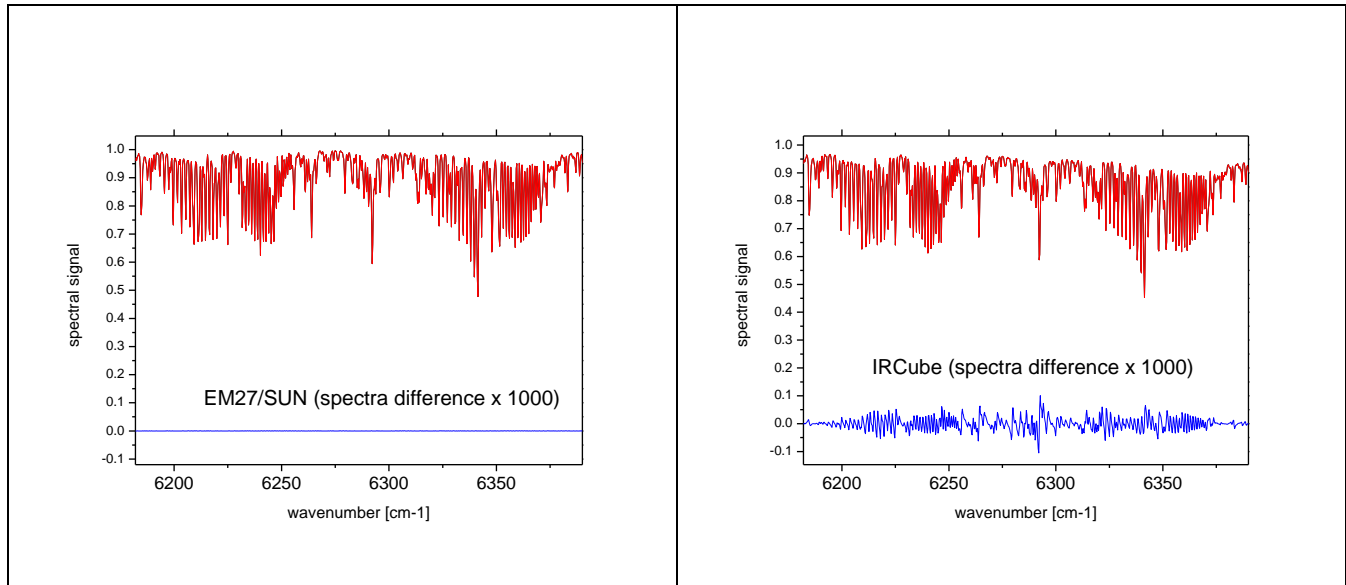


310
311 Figure 4: Vertex 70 phase spectrum. Left panel: raw phase (black) and fitted analytical phase (red). Right panel: difference
312 between model (analytical) and raw phase (raw). The gaps in the raw phase are due to opaque spectral sections.

313 314 315 5 Impact of the phase on the spectrum and on retrieved gas columns

316 Figure 5 shows the effect of using either the classical Mertz or the analytical phase when calculating the spectrum from the
317 measured interferogram in a non-opaque spectral region. We here use the EM27/SUN and the IRCube for illustration and we

318 investigate the spectral region used for the analysis of CO₂ (~ 6200 – 6400 cm⁻¹). The EM27/SUN phase spectrum is nearest
319 to a straight line, and the differences between Mertz and analytical phase are well within 1 mrad in the CO₂ region (see
320 Figure 1). The IRCube phase spectrum has stronger curvature, but the model used for the analytical phase still delivers a
321 good fit. The differences between Mertz and analytical phase are mostly within 2 mrad in the CO₂ region (see Figure 2).
322



323
324 Figure 5: differences of spectra as resulting from the Mertz phase correction scheme and the analytical phase approach. Left:
325 EM27/SUN, right: IRCube, the spectral residuals are enlarged by a factor of 1000.

326
327 According to Figure 5, the spectral differences of the IRCube spectra are significantly larger than for the EM27/SUN. This is
328 a reminder of the fact that double-sided interferogram recording has an important intrinsic advantage over single-sided
329 interferograms, because the propagation of a phase error into the spectrum is much more critical for single-sided
330 interferograms. While sine contributions emerging from $\pm OPD$ cancel out in double-sided interferograms, they give rise to
331 point-symmetric residuals around spectral lines in spectra generated from single-sided interferograms. Securing an optimized
332 phase reconstruction is of higher importance for single-sided interferograms (all the spectrometers investigated here apart
333 from the EM27/SUN) than for the EM27/SUN, which essentially is insensitive to phase errors in reasonable limits.

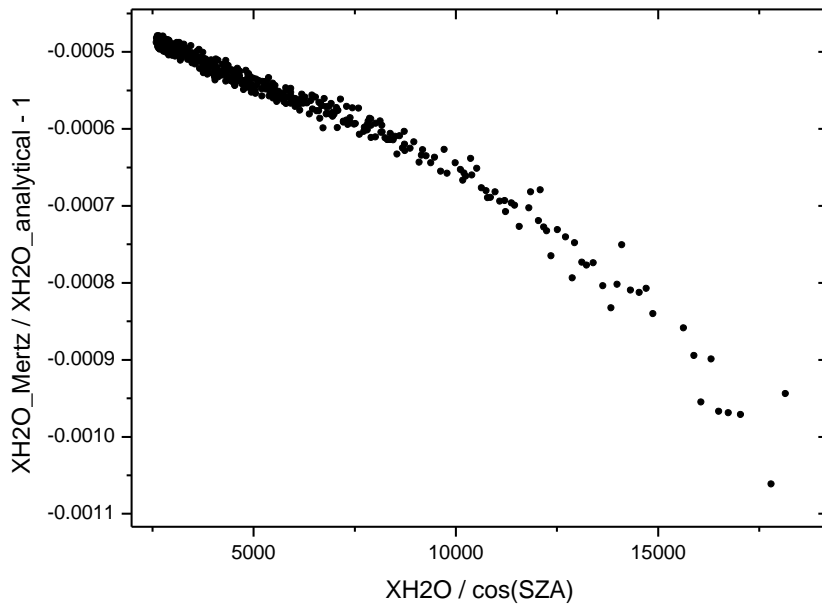
334
335 The spectral differences due to either using the analytical phase or the classical Mertz phase found for the IRCube are quite
336 moderate (below the 10^{-4} level). On the other hand both the increasing demands to be met for the validation of new space
337 borne GHG missions as well as the desired ability to quantify local sources from differential column measurements make
338 XCO₂ measurements with accuracies in the 0.05 ppm range desirable ($\sim 10^{-4}$). For example, Reißmann et al., 2022, state that

339 the XCO₂ gradients across the medium-sized city Munich typically are well below the 1 ppm level. Let us assume 0.5 ppm
340 as a typical signal amplitude and the uncertainty on the source strength estimate due to imperfect description of transport to
341 reside on the 20% level. In order to avoid a significant uncertainty contribution from the FTIR observation, we need an
342 accuracy level of $10\% \cdot 0.5 \text{ ppm} = 0.05 \text{ ppm}$.

343

344 The analysis of the IRcube spectra indicates a relative change of CO₂ column of about $2 \cdot 10^{-5}$ between the two phase
345 corrections methods, which is not expected to be of any relevance even if the aforementioned very stringent requirement for
346 XCO₂ accuracy is used..

347 However, the inspection of the phase spectra reveals that in near-opaque regions, the differences between raw (classical
348 Mertz) phase and the analytical phase becomes significantly larger. The 8730 – 8850 cm⁻¹ window is a nice study region for
349 this effect. This rather opaque region created by H₂O absorption resides isolated between transparent regions covered in the
350 same filter band, and the spectral flux is still sufficient for the determination of raw phase values inside the band. As
351 indicated by figures 2 and 4, the IRCube and the Vertex70 produce significant phase deviations in this spectral region (up to
352 90 mrad for the Vertex 70 and up to 25 mrad for the IRCube).



353

354 Figure 6: Relative difference of retrieved XH₂O from the 8730 – 8850 cm⁻¹ window, which resides in a strong H₂O
355 absorption band, using either the classical Mertz phase or the analytical phase for spectra generation. For the abscissa, the
356 product of H₂O abundance times airmass is used as a measure for the absorption strength.

357

358 Figure 6 shows the relative difference between IRCube XH₂O values retrieved from either classical Mertz phase corrected
359 spectra or from analytical phase corrected spectra. The abscissa shows the airmass-scaled H₂O abundance, which is
360 proportional to the H₂O slant column, providing a measure for saturation strength of the observed spectral band. The relative
361 difference of retrieved XH₂O for lower degree of saturation of the target species band starts around 0.5 per mil and reaches 1
362 per mil at higher solar zenith angles. This is a relevant result in the context of GHG measurements. The combination of the
363 currently used weak NIR bands with stronger MIR bands for further improving the information content of GHG retrievals is
364 currently under investigation by the networks. The performance of the classical Mertz phase correction is expected to be
365 suboptimal for the stronger MIR GHG bands.

366

367 In general, there is no guarantee that the analytical phase solution is nearer to the truth than the Mertz phase spectrum. The
368 results always need to be evaluated in context of the specific application. The analytical model might require extensions to
369 include unexpected phase oscillations (as for the Vertex 70). In any case, however, the analytical method is highly useful to
370 carve out unexpected structures in the Mertz phase, which are easily overlooked without performing a comparison to the
371 smooth analytical phase. A careful analysis of such features might help to further improve the design of interferometers and
372 supports recognition of instrumental problems, because the non-local spectral artefacts created by various error sources (as
373 nonlinearity, sampling ghosts, double passing) also create disturbances of the phase spectrum.

374

375 **6 Summary and Conclusion**

376 We have implemented a refined method for reconstructing the phase spectrum of FTIR spectrometers. We have applied the
377 new method to different types of spectrometers and found pronounced differences in phase imperfections between them. Our
378 findings demonstrate the usefulness of the method proposed both for operational work and instrumental diagnosis, especially
379 for saturated absorption bands. The proposed algorithm has been incorporated in the COCCON pre-processing code, which
380 is available under the GNU General Public License version 3.

381

382

383

384 **Authors Share**

385 FH has implemented the new method for phase correction using analytical model fits of the phase spectrum. He has
386 generated the results for the different spectrometers investigated in this work and wrote the predominant part of the
387 manuscript. All authors have studied and commented on the manuscript.

388

389 **Competing Interests**

390 At least one of the (co-)authors is a member of the editorial board of Atmospheric Measurement Techniques.

391

392 **Acknowledgements**

393 The establishment of the Izaña TCCON site was supported by grants from NASA's terrestrial carbon cycle program and
394 from the OCO project office.

395

396 **Financial Support**

397 This research has been supported by the European Space Agency (contract 400136108/21/I-DT-Ir).

398

399 **Code Availability**

400 The COCCON software suite including the pre-processing software PREPROCESS is made available under GPL version 3
401 license. From version 2.3 onwards, it supports the option of using the analytical phase model implemented in
402 PREPROCESS. The software suite and source codes are available for download at [https://www.imk-](https://www.imk-asf.kit.edu/english/3225.php)
403 [asf.kit.edu/english/3225.php](https://www.imk-asf.kit.edu/english/3225.php).

404

405 **References**

406

407 Alberti, C., Hase, F., Frey, M., Dubravica, D., Blumenstock, T., Dehn, A., Castracane, P., Surawicz, G., Harig, R., Baier, B.
408 C., Bès, C., Bi, J., Boesch, H., Butz, A., Cai, Z., Chen, J., Crowell, S. M., Deutscher, N. M., Ene, D., Franklin, J. E., García,
409 O., Griffith, D., Grouiez, B., Grutter, M., Hamdouni, A., Houweling, S., Humpage, N., Jacobs, N., Jeong, S., Joly, L., Jones,
410 N. B., Jouglet, D., Kivi, R., Kleinschek, R., Lopez, M., Medeiros, D. J., Morino, I., Mostafavipak, N., Müller, A., Ohyama,
411 H., Palmer, P. I., Pathakoti, M., Pollard, D. F., Raffalski, U., Ramonet, M., Ramsay, R., Sha, M. K., Shiomi, K., Simpson,
412 W., Stremme, W., Sun, Y., Tanimoto, H., Té, Y., Tsidu, G. M., Velazco, V. A., Vogel, F., Watanabe, M., Wei, C., Wunch,
413 D., Yamasoe, M., Zhang, L., and Orphal, J.: Improved calibration procedures for the EM27/SUN spectrometers of the

414 Collaborative Carbon Column Observing Network (COCCON), *Atmos. Meas. Tech.*, 15, 2433–2463,
415 <https://doi.org/10.5194/amt-15-2433-2022>, 2022.

416

417 P. F. Bernath, C. T. McElroy, M. C. Abrams, C. D. Boone, M. Butler, C. Camy-Peyret, M. Carleer, C. Clerbaux, P.-F.
418 Coheur, R. Colin, P. DeCola, M. DeMazière, J. R. Drummond, D. Dufour, W. F. J. Evans, H. Fast, D. Fussen, K.
419 Gilbert, D. E. Jennings, E. J. Llewellyn, R. P. Lowe, E. Mahieu, J. C. McConnell, M. McHugh, S. D. McLeod, R.
420 Michaud, C. Midwinter, R. Nassar, F. Nichitiu, C. Nowlan, C. P. Rinsland, Y. J. Rochon, N. Rowlands, K. Semeniuk,
421 P. Simon, R. Skelton, J. J. Sloan, M.-A. Soucy, K. Strong, P. Tremblay, D. Turnbull, K. A. Walker, I. Walkty, D. A.
422 Wardle, V. Wehrle, R. Zander, and J. Zou: Atmospheric Chemistry Experiment (ACE): Mission overview, *Geophys. Res.*
423 *Let.*, 32, L15S01, doi:10.1029/2005GL022386, 2005.

424

425 Brasunas, J. C. and Cushman, G. M.: Uniform Time sampling Fourier Transform Spectroscopy, *Appl. Optics*, 36, 2206–
426 2210, doi:10.1364/AO.36.002206, 1997.

427

428 Brault, J. W.: New approach to high-precision Fourier transform spectrometer design, *Appl. Optics*, 35, 2891–2896,
429 doi:10.1364/AO.35.002891, 1996.

430

431 Davis, S. P., Abrams, M. C. & Brault, J. W. *Fourier Transform Spectrometry*, Academic Press, San Diego, 2001.

432

433 De Mazière, M., Thompson, A. M., Kurylo, M. J., Wild, J. D., Bernhard, G., Blumenstock, T., Braathen, G. O., Hannigan, J.
434 W., Lambert, J.-C., Leblanc, T., McGee, T. J., Nedoluha, G., Petropavlovskikh, I., Seckmeyer, G., Simon, P. C., Steinbrecht,
435 W., and Strahan, S. E.: The Network for the Detection of Atmospheric Composition Change (NDACC): history, status and
436 perspectives, *Atmos. Chem. Phys.*, 18, 4935–4964, <https://doi.org/10.5194/acp-18-4935-2018>, 2018.

437

438 Farmer, Crofton B.: High resolution infrared spectroscopy of the sun and the earth's atmosphere from space. *Mikrochimica*
439 *Acta*, 93, 189-214 doi:10.1007/bf01201690, 1987

440

441 Fischer, H., Birk, M., Blom, C., Carli, B., Carlotti, M., von Clarmann, T., Delbouille, L., Dudhia, A., Ehhalt, D., Endemann,
442 M., Flaud, J. M., Gessner, R., Kleinert, A., Koopman, R., Langen, J., López-Puertas, M., Mosner, P., Nett, H., Oelhaf, H.,
443 Perron, G., Remedios, J., Ridolfi, M., Stiller, G., and Zander, R.: MIPAS: an instrument for atmospheric and climate
444 research, *Atmos. Chem. Phys.*, 8, 2151–2188, <https://doi.org/10.5194/acp-8-2151-2008>, 2008.

445

446 Forman, M. L., Steel, W. H. & Vanasse, G. A. Correction of asymmetric interferograms obtained in Fourier spectroscopy. *J.*
447 *Opt. Soc. Am.* 56, 59–63, 1966.

448

449 Frey, M., Sha, M. K., Hase, F., Kiel, M., Blumenstock, T., Harig, R., Surawicz, G., Deutscher, N. M., Shiomi, K., Franklin,
450 J. E., Bösch, H., Chen, J., Grutter, M., Ohyama, H., Sun, Y., Butz, A., Mengistu Tsidu, G., Ene, D., Wunch, D., Cao, Z.,
451 García, O., Ramonet, M., Vogel, F., and Orphal, J.: Building the COllaborative Carbon Column Observing Network
452 (COCCON): long-term stability and ensemble performance of the EM27/SUN Fourier transform spectrometer, *Atmos.*
453 *Meas. Tech.*, 12, 1513-1530, <https://doi.org/10.5194/amt-12-1513-2019>, 2019.

454

455 Friedl-Vallon, F., Gulde, T., Hase, F., Kleinert, A., Kulesa, T., Maucher, G., Neubert, T., Olschewski, F., Piesch, C.,
456 Preusse, P., Rongen, H., Sartorius, C., Schneider, H., Schönfeld, A., Tan, V., Bayer, N., Blank, J., Dapp, R., Ebersoldt, A.,
457 Fischer, H., Graf, F., Guggenmoser, T., Höpfner, M., Kaufmann, M., Kretschmer, E., Latzko, T., Nordmeyer, H., Oelhaf, H.,
458 Orphal, J., Riese, M., Schardt, G., Schillings, J., Sha, M. K., Suminska-Ebersoldt, O., and Ungermann, J.: Instrument concept
459 of the imaging Fourier transform spectrometer GLORIA, *Atmos. Meas. Tech.*, 7, 3565–3577, [https://doi.org/10.5194/amt-7-](https://doi.org/10.5194/amt-7-3565-2014)
460 [3565-2014](https://doi.org/10.5194/amt-7-3565-2014), 2014.

461

462 García, O. E., Schneider, M., Sepúlveda, E., Hase, F., Blumenstock, T., Cuevas, E., Ramos, R., Gross, J., Barthlott, S.,
463 Röhling, A. N., Sanromá, E., González, Y., Gómez-Peláez, Á. J., Navarro-Comas, M., Puentedura, O., Yela, M., Redondas,
464 A., Carreño, V., León-Luis, S. F., Reyes, E., García, R. D., Rivas, P. P., Romero-Campos, P. M., Torres, C., Prats, N.,
465 Hernández, M., and López, C.: Twenty years of ground-based NDACC FTIR spectrometry at Izaña Observatory – overview
466 and long-term comparison to other techniques, *Atmos. Chem. Phys.*, 21, 15519–15554, [https://doi.org/10.5194/acp-21-](https://doi.org/10.5194/acp-21-15519-2021)
467 [15519-2021](https://doi.org/10.5194/acp-21-15519-2021), 2021.

468

469 Gisi, M., Hase, F., Dohe, S., and Blumenstock, T.: Camtracker: a new camera controlled high precision solar tracker system
470 for FTIR-spectrometers, *Atmos. Meas. Tech.*, 4, 47–54, <https://doi.org/10.5194/amt-4-47-2011>, 2011.

471

472 Gisi, M., Hase, F., Dohe, S., Blumenstock, T., Simon, A., and Keens, A.: XCO₂-measurements with a Tabletop FTS Using
473 Solar Absorption Spectroscopy, *Atmospheric Measurement Techniques*, 5, 2969–2980, [https://doi.org/10.5194/amt-5-2969-](https://doi.org/10.5194/amt-5-2969-2012)
474 [2012](https://doi.org/10.5194/amt-5-2969-2012), 2012.

475

476 Griffiths, P. R., and De Haseth, J. A.: *Fourier Transform Infrared Spectrometry*, John Wiley & Sons Inc., Hoboken, 2007.

477

478 Hase, F., T. Blumenstock, C. Paton-Walsh: Analysis of the instrumental line shape of high-resolution Fourier transform IR
479 spectrometers with gas cell measurements and new retrieval software, *Appl. Opt.* 38, 3417-3422, 1999

480

481 Hase, F., M. Frey, M. Kiel, T. Blumenstock, R. Harig, A. Keens, and J. Orphal: Addition of a channel for XCO observations
482 to a portable FTIR spectrometer for greenhouse gas measurements, *Atmos. Meas. Tech.*, 9, 2303-2313, doi:10.5194/amt-9-
483 2303-2016, 2016.

484

485 Hase, F., M. Frey, T. Blumenstock, J. Groß, M. Kiel, R. Kohlhepp, G. Mengistu Tsidu, K. Schäfer, M. K. Sha, and J. Orphal:
486 Application of portable FTIR spectrometers for detecting greenhouse gas emissions of the major city Berlin, *Atmos. Meas.*
487 *Tech.*, 8, 3059-3068, doi:10.5194/amt-8-3059-2015, 2015.

488

489 Herres, W. & Gronholz, J. Understanding FT-IR data processing. Part 2: Details of the spectrum calculation. *Intell. Instrum.*
490 *Comput., Appl. Lab.* 3, 10–19, 1985.

491

492 Kille, N., Chiu, R., Frey, M., Hase, F., Sha, M. K., Blumenstock, T., Hannigan, J.W., Orphal, J.W., Bon, D. and Volkamer,
493 R.: Separation of methane emissions from agricultural and naturalgas sources in the Colorado Front Range, *Geophysical*
494 *Research Letters*, 46, <https://doi.org/10.1029/2019GL08213>, 2019.

495

496 Richard C. M. Learner, Anne P. Thorne, Ian Wynne-Jones, James W. Brault, and Mark C. Abrams: Phase correction of
497 emission line Fourier transform spectra, *J. Opt. Soc. Am. A* 12, 2165-2171, 1995.

498

499 Luther, A., Kleinschek, R., Scheidweiler, L., Defratyka, S., Stanisavljevic, M., Forstmaier, A., Dandocsi, A., Wolff, S.,
500 Dubravica, D., Wildmann, N., Kostinek, J., Jöckel, P., Nickl, A.-L., Klausner, T., Hase, F., Frey, M., Chen, J., Dietrich, F.,
501 Nęcki, J., Swolkień, J., Fix, A., Roiger, A., and Butz, A.: Quantifying CH₄ emissions from hard coal mines using mobile
502 sun-viewing Fourier transform spectrometry, *Atmos. Meas. Tech.*, 12, 5217–5230, [https://doi.org/10.5194/amt-12-5217-](https://doi.org/10.5194/amt-12-5217-2019)
503 2019, 2019.

504

505 Luther, A., Kostinek, J., Kleinschek, R., Defratyka, S., Stanisavljević, M., Forstmaier, A., Dandocsi, A., Scheidweiler, L.,
506 Dubravica, D., Wildmann, N., Hase, F., Frey, M. M., Chen, J., Dietrich, F., Nęcki, J., Swolkień, J., Knote, C., Vardag, S. N.,
507 Roiger, A., and Butz, A.: Observational constraints on methane emissions from Polish coal mines using a ground-based
508 remote sensing network, *Atmos. Chem. Phys.*, 22, 5859–5876, <https://doi.org/10.5194/acp-22-5859-2022>, 2022.

509

510 Mertz, L., *Transformations in Optics*, John Wiley and Sons, Inc., New York, 1965.

511

512 Reißmann, M., Chen, J., Osterman, G., Zhao, X., Dietrich, F., Makowski, M., Hase, F., and Kiel, M.: Comparison of OCO-2
513 target observations to MUCCnet – is it possible to capture urban X_{CO2} gradients from space?, *Atmos. Meas. Tech.*, 15, 6605–
514 6623, <https://doi.org/10.5194/amt-15-6605-2022>, 2022.

515

516 Schneider, M., Blumenstock, T., Chipperfield, M. P., Hase, F., Kouker, W., Reddman, T., Ruhnke, R., Cuevas, E., and
517 Fischer, H.: Subtropical trace gas profiles determined by groundbased FTIR spectroscopy at Izaña (28° N, 16° W): Five-year
518 record, error analysis, and comparison with 3-D CTMs, *Atmos. Chem. Phys.*, 5, 153–167, [https://doi.org/10.5194/acp-5-](https://doi.org/10.5194/acp-5-153-2005)
519 153-2005, 2005.

520

521 Schneider, M., Sepúlveda, E., García, O., Hase, F., and Blumenstock, T.: Remote sensing of water vapour profiles in the
522 framework of the Total Carbon Column Observing Network (TCCON), *Atmos. Meas. Tech.*, 3, 1785–1795,
523 <https://doi.org/10.5194/amt-3-1785-2010>, 2010.

524

525 Sha, M. K., De Mazière, M., Notholt, J., Blumenstock, T., Chen, H., Dehn, A., Griffith, D. W. T., Hase, F., Heikkinen, P.,
526 Hermans, C., Hoffmann, A., Huebner, M., Jones, N., Kivi, R., Langerock, B., Petri, C., Scolas, F., Tu, Q., and Weidmann,
527 D.: Intercomparison of low- and high-resolution infrared spectrometers for ground-based solar remote sensing measurements
528 of total column concentrations of CO₂, CH₄, and CO, *Atmos. Meas. Tech.*, 13, 4791–4839, [https://doi.org/10.5194/amt-13-](https://doi.org/10.5194/amt-13-4791-2020)
529 4791-2020, 2020.

530

531 M.K. Sha et al., Remote Sensing 2024 (Manuscript ID: remotesensing-3148670) submitted on 25 July 2024.

532

533 Tu, Q., Hase, F., Schneider, M., García, O., Blumenstock, T., Borsdorff, T., Frey, M., Khosrawi, F., Lorente, A., Alberti, C.,
534 Bustos, J. J., Butz, A., Carreño, V., Cuevas, E., Curcoll, R., Diekmann, C. J., Dubravica, D., Ertl, B., Estruch, C., León-Luis,
535 S. F., Marrero, C., Morgui, J.-A., Ramos, R., Scharun, C., Schneider, C., Sepúlveda, E., Toledano, C., and Torres, C.:
536 Quantification of CH₄ emissions from waste disposal sites near the city of Madrid using ground- and space-based
537 observations of COCCON, TROPOMI and IASI, *Atmos. Chem. Phys.*, 22, 295–317, [https://doi.org/10.5194/acp-22-295-](https://doi.org/10.5194/acp-22-295-2022)
538 2022, 2022.

539

540 D. Wunch, G.C. Toon, J.-F.L. Blavier, R.A. Washenfelder, J. Notholt, B.J. Connor, D.W.T. Griffith, V. Sherlock, P.O.
541 Wennberg. The Total Carbon Column Observing Network. *Phil. Trans. R. Soc. A*, 369, doi:10.1098/rsta.2010.0240, 2011.

542

543 Yokota, T., Yoshida, Y., Eguchi, N., Ota, Y., Tanaka, T., Watanabe, H., and Maksyutov, S.: Global Concentrations of CO₂
544 and CH₄ Retrieved from GOSAT: First Preliminary Results, *SOLA*, 5, 160–163, <https://doi.org/10.2151/sola.2009-041>,
545 2009.

546

547 M. Zhou, B. Langerock, M. K. Sha, C. Hermans, N. Kumps, R. Kivi, P. Heikkinen, C. Petri, J. Notholt, H. Chen, and M. De
548 Mazière. Atmospheric n₂o and ch₄ total columns retrieved from low-resolution fourier transform infrared (ftir) spectra

549 (bruker vertex 70) in the mid-infrared region. *Atmospheric Measurement Techniques*, 16 (22): 5593–5608, 2023. doi:
550 10.5194/amt-16-5593-2023.
551